Chemical Science

ROYAL SOCIETY OF CHEMISTRY

EDGE ARTICLE

View Article Online
View Journal | View Issue

Check for updates

Cite this: *Chem. Sci.*, 2020, **11**, 8885

All publication charges for this article have been paid for by the Royal Society of Chemistry

Coordinative-to-covalent transformation, isomerization dynamics, and logic gate application of dithienylethene based photochromic cages†

Jian-Hua Zhang,[a] Hai-Ping Wang,[b] Lu-Yin Zhang,[a] Shi-Chao Wei,[a] Zhang-Wen Wei,[a] Mei Pan *[a] and Cheng-Yong Su*[a]

Received 14th June 2020
Accepted 5th August 2020

DOI: 10.1039/d0sc03290e

rsc.li/chemical-science

Photochromic coordinative cages containing dynamic C=N imine bonds are assembled from a dithienylethene-based aldehyde and tris-amine precursors *via* metallo-component self-assembly. The resulting metal-templated cages are then reduced and demetalated into pure covalent-organic cages (COCs), which are otherwise difficult to prepare *via de novo* organic synthesis. Both the obtained coordinative and covalent cages can be readily interconverted between the ring-open (*o*-isomer) and one-lateral ring-closed (*c*-isomer) forms by UV/vis light irradiation, demonstrating distinct absorption, luminescence and photoisomerization dynamics. Specifically, the ring-closed *c*-COCs show a blue-shifted absorption band compared with analogous metal-templated cages, which can be applied in photoluminescence (PL) color-tuning of upconversion materials in different ways, showing potential for constructing multi-readout logic gate systems.

Open Access Article. Published on 06 August 2020. Downloaded on 2/6/2026 6:47:13 AM.
This article is licensed under a Creative Commons Attribution-NonCommercial 3.0 Unported Licence.

Introduction

One-pot component self-assembly of versatile coordination architectures has aroused great interest in recent years. In particular, *via* the synergetic formation of dynamic covalent imine bonds (C=N) and coordination bonds, a variety of fascinating structures have been constructed, including cages,[1–12] helicates,[13–16] capsules,[17–20] borromeates,[21–23] catenanes[24–27] and rotaxanes.[28–31] Multi-component self-assembly of pure covalent-organic cage-like architectures with well-defined complexity and integrity has been achieved,[32–35] but the use of metallo-components may provide further control of the process by preorientation through metal ion coordination. This strategy takes advantage of a predefined metal-templated architecture in the formation of multiple imine bonds during the synergistic self-assembly process, and the resulting generated dynamic constituents can be reduced to demetalated non-dynamic organic analogues which are not anymore subject to reversible deconstruction. Such coordinative-to-covalent transformation leads to pure covalent-organic cage-like ensembles with specific chemical stability, solubility, flexibility, guest-binding capacity, and so on, in comparison with their coordinative counterparts, thereof giving access to new practical applications.

Owing to the light-induced open- and closed-ring isomerization, dithienylethene (DTE)-type photochromic materials have attracted broad interest for their extensive application in switching devices, optical memories, optoelectronics, magnetics, bio-imaging and therapy, *etc.*[36–41] Among which, it is intriguing to employ the specific photo-responsiveness of DTE to build composite logical operating systems on a molecular or supramolecular level. For this purpose, various organics, organometallics, and metal–organic supramolecular or hybrid systems have been designed, including some wonderful work such as the light-switchable coordination cages reported by Clever and so on.[42–44] In these studies, the formation and photoswitching behaviour of metal–organic cages have been reported to incorporate similar dithienylethene moieties. However, to the best of our knowledge, the integration of multiple light-switchable DTE components into well-defined organic cages has less been explored. This might be achieved by the above proposed strategy of coordinative-to-covalent structural conversion from one-pot component self-assembly of photochromic metal-templated cages, followed by reduction and demetalation to covalent-organic cages (COCs). Along this line, detailed comparison of the switching behaviours between ligands, organic cages and coordinative cages can be performed, and then applied for potential optical storage and processing functionalities.

In this work, a new DTE-based photochromic molecule, 5,5′-(4,4′-(cyclopentene-1,2-diyl)bis(5-methylthiophene-4,2-diyl))

[a]*MOE Laboratory of Bioinorganic and Synthetic Chemistry, Lehn Institute of Functional Materials, School of Chemistry, Sun Yat-Sen University, Guangzhou 510275, China. E-mail: panm@mail.sysu.edu.cn; cesscy@mail.sysu.edu.cn*

[b]*School of Biotechnology and Health Sciences, Wuyi University, Jiangmen 529020, China*

† Electronic supplementary information (ESI) available: Materials and instruments, experimental details, more NMR, MS and photophysical spectra, and crystal data. CCDC 1917232–1917235, 1917798, 1919654 and 1922928. For ESI and crystallographic data in CIF or other electronic format see DOI: 10.1039/d0sc03290e

Open Access Article. Published on 06 August 2020. Downloaded on 2/6/2026 6:47:13 AM.
This article is licensed under a Creative Commons Attribution-NonCommercial 3.0 Unported Licence.

dipicolin-aldehyde (PADTE, L), tris(2-aminoethyl)amine or tris(2-aminopropyl)amine (A^1 or A^2), and Zn^{II}/Cd^{II} ions were applied for component self-assembly to afford $A_2L_3M_2$-type metal-templated cages. Upon reduction of the imine bonds by $NaBH_4$, the as-prepared cages can be demetalated to afford metal-free R-A_2L_3 COCs (R means a reduced form). Both coordinative and covalent cages are able to undergo reversible ring-opening/closing isomerization upon UV/vis irradiation, yet only one DTE-lateral side among the three is found to be "closed" as revealed by single-crystal structure and solution UV/NMR

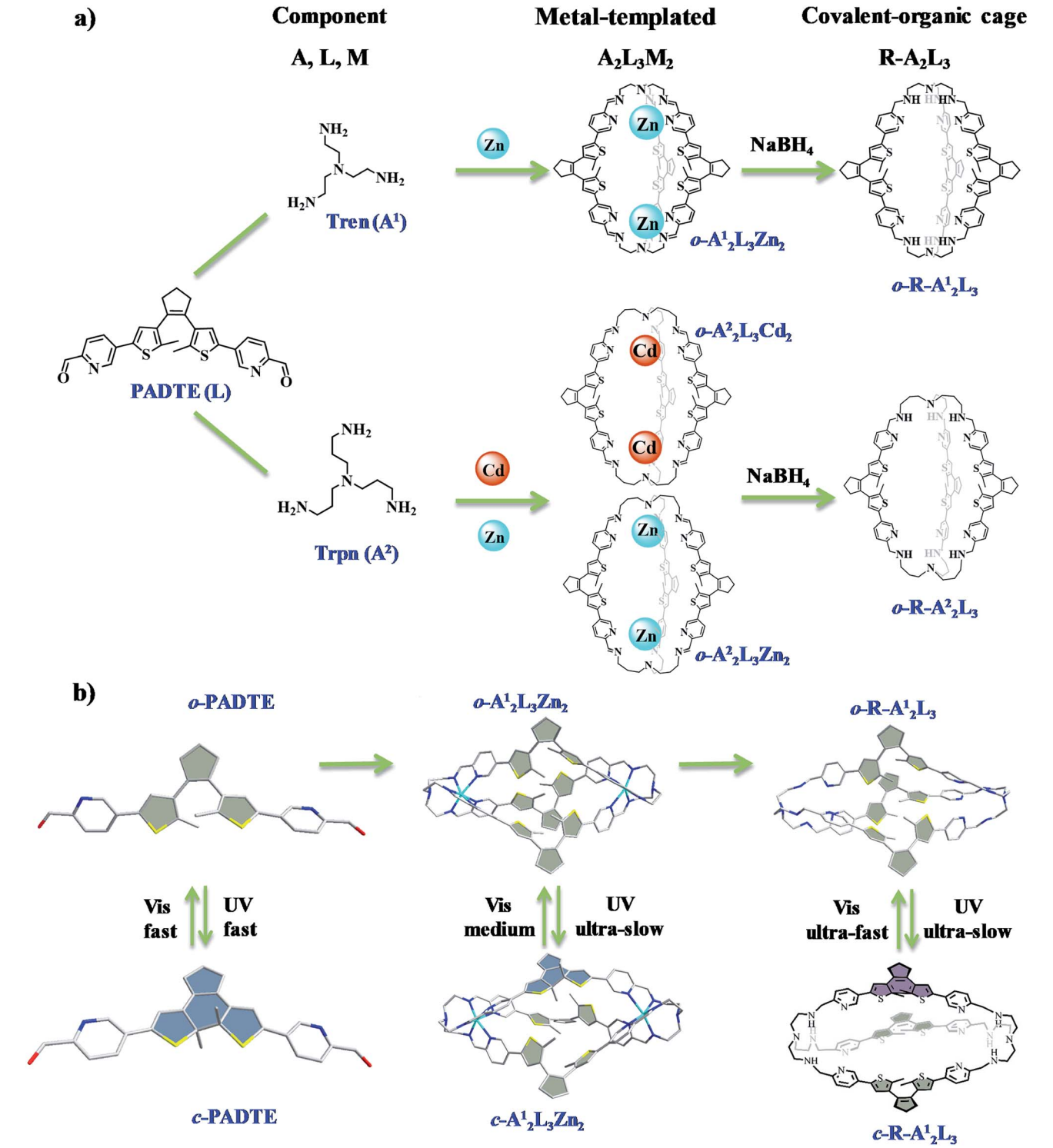

Scheme 1 (a) Component self-assembly of photo-responsive $A_2L_3M_2$ (A = A^1 or A^2, M = Zn^{II} or Cd^{II}) metal-templated cages, and further reduction into R-A_2L_3 covalent-organic cages. (b) UV/vis induced ring-opening/closing behaviors in PADTE, $A^1_2L_3Zn_2$, and R-$A^1_2L_3$ with different photoisomerization dynamics.

This journal is © The Royal Society of Chemistry 2020

Open Access Article. Published on 06 August 2020. Downloaded on 2/6/2026 6:47:13 AM.
This article is licensed under a Creative Commons Attribution-NonCommercial 3.0 Unported Licence.

detection. The photoisomerization dynamic rates and potential application of the cages in PL color-tuning of upconversion materials for logic gate operations are then studied.

Results and discussion

Component self-assembly of open-ring metal-templated cages

Photo-switchable organic precursor PADTE was synthesized from 1,2-bis(5-chloro-2-methyl-3-thienyl)cyclopentene and 5-bromopicolinaldehyde (Scheme S1, Tables S1–3, and Fig. S1–S4†).[45] The one-pot reaction of PADTE (L), tris(2-aminoethyl) amine (Tren, A^1) and zinc triflate afforded the *o*-$A^1_2L_3Zn_2$ cage, while changing Tren to tris(2-aminopropyl)amine (Trpn, A^2) to react with PADTE and corresponding metal triflates led to assembly of *o*-$A^2_2L_3Zn_2$ and *o*-$A^2_2L_3Cd_2$ cages (Scheme 1), as confirmed by solution NMR, ESI-MS, and solid-state IR and single-crystal determination (Fig. S5–S22†).

The single-crystals of *o*-$A^1_2L_3Zn_2$ and *o*-$A^2_2L_3Cd$ suitable for X-ray diffraction analysis were obtained by natural evaporation of CH_3CN solution or diffusion of ether into the CH_3CN solution of corresponding complexes, respectively. As seen in Fig. 1 and Tables S4–S9,† *o*-$A^1_2L_3Zn_2$ with a formula of $[A^1_2L_3Zn_2]\cdot(CF_3SO_3)_4\cdot 3CH_3CN\cdot 15H_2O$ crystallizes in the triclinic *P*-1 space group, forming a triple-helicate cage structure with all three PADTE-laterals taking open-ring isomeric configuration. The exterior skeleton of *o*-$A^1_2L_3Zn_2$ is sustained by covalent bonds due to *in situ* formation of dynamic C=N imine bonds upon coalescence of the three PADTE laterals with two triamine toppings, forming three sets of N^N chelators (one pyridine N and one imine N) on each end to wrap around a Zn^{2+} center. In this sense, the *o*-$A^1_2L_3Zn_2$ cage can be considered as a prototype pre-organized for a pure organic cage. Two Zn^{2+} ions serve as the templates during cage assembly, directing the formation of dynamic imine bonds through coordination with the three $(N^{\wedge}N)_3$ chelators in a distorted octahedral geometry. Due to the propeller-arrangement of the three coordinated pyridine rings and triamine arms, Δ- or Λ-stereo-configuration is generated around each Zn^{2+} center. In each *o*-$A^1_2L_3Zn_2$ cage, the two coordination ends have the same kind of stereo-configuration, forming ΔΔ- or ΛΛ-homochiral cage molecules. However, in the crystal lattice, the two kinds of stereoisomeric cages with opposite handedness coexist, giving rise to a racemic crystal (Fig. S12†). The three PADET laterals of *o*-$A^1_2L_3Zn_2$ take a twisted mode, all in the open-ring configuration. Nevertheless, a geometric difference can be found in their orientation of the two thiophene rings, leading to disparity in the distance between C···C atoms potential for the ring-closing photoreaction (3.52, 3.48 and 3.34 Å), which become differentiable by the ^{1}H NMR signals when a light-induced ring-closing process occurs as discussed below. The Zn–Zn distance within the cage is 16.21 Å. A similar triple-helicate cage was revealed by the single-crystal strucure of *o*-$A^2_2L_3Cd$ with a formula of $[A^2_2L_3Cd_2]\cdot(CF_3SO_3)_4\cdot$solvents, except for the replacement of metal centers by Cd^{2+} and cage toppings by tris(2-aminopropyl)amine (Trpn, A^2). Due to the longer propyl linker in A^2, a slightly larger inner cavity is formed in *o*-$A^2_2L_3Cd_2$, in which the Cd–Cd distance is 16.49 Å (Fig. S19†). It is worth noting that the single-crystal of *o*-$A^2_2L_3Cd_2$ is in a chiral space group $P4_32_12$, indicating that the same handed cages prefer to cocrystallize to form a homochiral single-crystal and the whole product will be a crystal racemate.

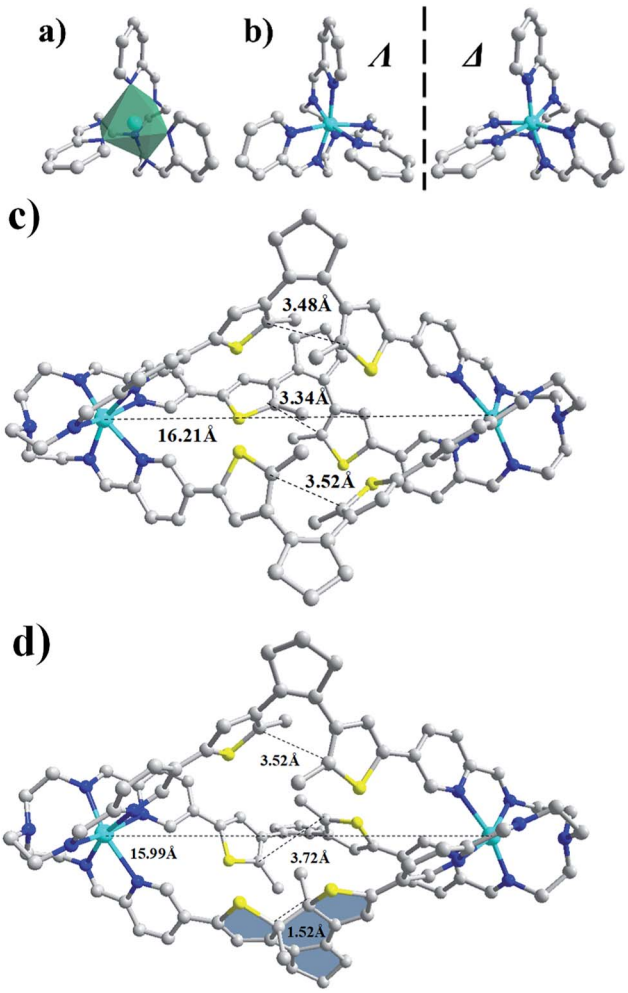

Fig. 1 Single-crystal structures of *o*-$A^1_2L_3Zn_2$ and *c*-$A^1_2L_3Zn_2$ cages. (a) Coordination geometry of Zn^{II}, (b) a pair of enantiomeric $Zn(N^{\wedge}N)_3$ coordination units with opposite Λ- or Δ-stereo-configurations, (c) ΛΛ-enantiomeric cage in *o*-$A^1_2L_3Zn_2$, (d) ΛΛ-enantiomeric cage in *c*-$A^1_2L_3Zn_2$ (grey for C, blue for N, yellow for S, and cyan for Zn, the closed PADTE-lateral shown in shadow, and H atoms, solvents and counter anions omitted for clarity).

The open-ring structures for the coordinative cages were also detected in a solution state. As shown in Fig. 2a and b for *o*-$A^1_2L_3Zn_2$, after one-pot component self-assembly, the original aldehyde proton signal (Ha) disappears while a new signal corresponding to the dynamic imine C=N bond (Ha′) appears, unveiling the formation of the *o*-$A^1_2L_3Zn_2$ cage. Assignment of other protons on the cage is confirmed from ^{1}H–^{1}H COSY and HSQC spectra (Fig. S8 and S9†). The high resolution ESI-MS spectrum of *o*-$A^1_2L_3Zn_2$ exhibits the peaks corresponding to $[(A^1_2L_3Zn_2) + CF_3SO_3^-]^{3+}$ and $[(A^1_2L_3Zn_2) + 2CF_3SO_3^-]^{2+}$ species, showing perfect agreement between the measured and simulated isotopic distributions (Fig. S10†). The DOSY spectrum (Fig. S11†) also supports the formation of a uniform cage

Open Access Article. Published on 06 August 2020. Downloaded on 2/6/2026 6:47:13 AM.
This article is licensed under a Creative Commons Attribution-NonCommercial 3.0 Unported Licence.

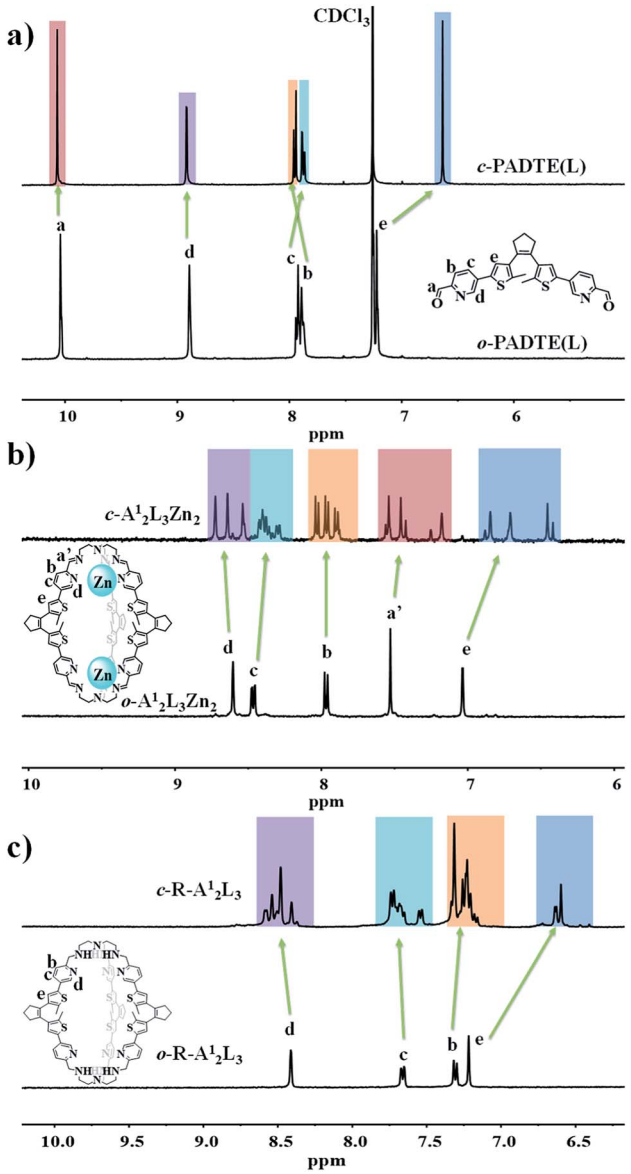

Fig. 2 ^{1}H NMR spectra of photochromic ligands *o*/*c*-PADTE in $CDCl_3$ (a), coordinative cages *o*/*c*-$A^1_2L_3Zn_2$ in CD_3CN (b), and covalent cages *o*/*c*-R-$A^1_2L_3$ in CD_3OD (c).

structure as seen from the identical diffusion coefficients (D), suggesting a cage with a solvodynamic radius of 9.4 Å according to a D value of 6.31×10^{-10} m^2 s^{-1}. The solution structures of *o*-$A^2_2L_3Zn_2$ and *o*-$A^2_2L_3Cd_2$ are similar to that of *o*-$A^1_2L_3Zn_2$, of which the spectroscopic characterization data are compiled in Fig. S13–S22 and Table S10.† A noteable finding is that, the geometric difference of the three PADET laterals in *o*-$A^1_2L_3Zn_2$, as revealed in the solid-state by single-crystal analysis, is not manifested by ^{1}H NMR signals, which is due to the fast equilibrium among the three components of the cage in the solution-state within the NMR timescale. However, when a ring-closing procedure takes place, obviously distinct proton signals can be observed for the cages but not for the PADET ligand (Fig. 2a and b, *vide infra*).

Reduction of coordinative cages to covalent cages

Pure organic cages could display better chemical stability, solubility and flexibility than coordinative cages, but their synthesis is usually tedious with low yield. Therefore, a convenient method is to use the self-assembled coordinative cages *o*-$A^1_2L_3Zn_2$ and *o*-$A^2_2L_3M_2$ (Zn/Cd) as precursors for pure organic cages to retain the overall cage shape and size. By reduction of the imine bonds into amine bonds with $NaBH_4$ under alkaline conditions, the templating metal centers can be simultaneously removed from the cages, resulting in pure covalent-organic cages *o*-R-$A^1_2L_3$ and *o*-R-$A^2_2L_3$ (Scheme 1). The successful acquisition of the *o*-R-$A^1_2L_3$ cage from the *o*-$A^1_2L_3Zn_2$ precursor was confirmed by NMR, HRMS, and IR measurements (Fig. S23–S27†). As shown in Fig. 2c, there are only four sets of peaks in the aromatic ring zone. Compared with the ^{1}H NMR spectra of *o*-$A^1_2L_3Zn_2$, the original imine proton signal disappears, proving the complete formation of *o*-R-$A^1_2L_3$. The DOSY spectrum (Fig. S26†) also supports the formation of a uniform cage structure as seen from the identical diffusion coefficients (D). The High resolution ESI-MS spectrum of *o*-R-$A^1_2L_3$ exhibits the peaks corresponding to $[(\text{R-A}^1_2\text{L}_3) + 2\text{H}^+]^{2+}$, $[(\text{R-A}^1_2\text{L}_3) + 3\text{H}^+]^{3+}$ and $[(\text{R-A}^1_2\text{L}_3) + \text{H}^+]^{4+}$ species with perfect agreement between the measured and simulated isotopic distributions (Fig. S27†). The definite structural information of *o*-R-$A^1_2L_3$ was established by the single-crystal diffraction analysis, which verifies the reduction of imine bonds and retention of triple-helicate cage resembling *o*-$A^1_2L_3Zn_2$ (Fig. S28 and Tables S11–S13†). The reduction of *o*-$A^2_2L_3Cd_2$ into *o*-R-$A^2_2L_3$ also gave similar results, confirming the success of the above reduction and demetalation method to obtain analogous *o*-R-$A^2_2L_3$ (Fig. S29–S34†).

Ring opening-closing photoisomerization processes of the PADTE ligand

The PADTE ligand (L) interconverts smoothly between open-ring (*o*-PADTE) and closed-ring (*c*-PADTE) forms upon UV (365 nm) and visible light (>455 nm) irradiation. The conversion from light colored solution of *o*-PADTE to blue solution of *c*-PADTE can be detected clearly by the naked eye (Fig. S35†). The transition happens quickly by the irradiation of a 365 nm UV light, as indicated by the shift of the proton signal on the thiophene ring from 7.2 ppm in *o*-PADTE to 6.7 ppm in *c*-PADTE (Fig. 2a and S36†). The photochromic process has been monitored by typical UV-Vis absorption evolution, in which the peak at 375 nm for *o*-PADTE gradually decreased, while two new peaks at 300 and 600 nm appear and steadily increase under UV irradiation, which darkens the solution color to reach the *c*-PADTE state (Fig. S37†). And a reverse process happens for *c*-PADTE under visible light irradiation, which is also testified by the color change and UV-Vis absorption evolution (Fig. S38†). The photoluminescence change of the PADTE ligand during the ring-closing process was also detected. As shown in Fig. S41,† *o*-PADTE shows a broad emission with the maximum at 570 nm (τ = 0.3 ns), which is gradually quenched by UV irradiation during ring-closing. The single-crystal structures of open/closed-ring forms are obtained (Scheme 1b and Tables S1–S3†), unambiguously confirming the photochromic isomerization.

This journal is © The Royal Society of Chemistry 2020

Open Access Article. Published on 06 August 2020. Downloaded on 2/6/2026 6:47:13 AM.
This article is licensed under a Creative Commons Attribution-NonCommercial 3.0 Unported Licence.

Metal-templated coordinative cages

The photochromic transition process from *o*-$A^1_2L_3Zn_2$ to *c*-$A^1_2L_3Zn_2$ was then studied by UV-Vis spectroscopy (Fig. 3 and S42†), and a similar photochromic phenomenon to the PADTE ligand was detected. In the open-ring form of the cage in $CH_3CN/CHCl_3$ solution, two absorption peaks at 253 and 374 nm dominate, consistent with the π–π* transitions of open-state PADTE. With prolonging of UV irradiation, the intensities of these two peaks diminish steadily, and two new peaks at 300 and 627 nm appear and increase gradually. These two peaks are correlated with the closed-ring form of PADTE. After UV irradiation (365 nm) for about 60 minutes, the UV-Vis spectrum of *o*-$A^1_2L_3Zn_2$ reaches a steady state, indicative of stopping of structural conversion. However, according to the absorption magnitude of the changing ratio compared to that of the PADTE ligand, it is deduced that only one of the three PADTE-laterals in the coordinative cage is closed. This implies a spatial hindrance for complete ring-closing in the cage structure, in which, after one lateral is closed, the other two laterals are blocked for closing due to high energy of configuration tension.

To confirm this speculation, the single-crystal of *c*-$A^1_2L_3Zn_2$ was grown by diffusing ether into the CH_3CN solution of *o*-$A^1_2L_3Zn_2$ after irradiation under UV light for three hours. Dark blue crystals of *o*-$A^1_2L_3Zn_2$ with a formula of $[A^1_2L_3Zn_2]\cdot(CF_3SO_3)_4\cdot$solvents were obtained after three days. As shown in Fig. 1, S46 and Table S4,† *c*-$A^1_2L_3Zn_2$ crystallizes in the monoclinic $P2_1/n$ space group, forming a similar triple-helicate cage to *o*-$A^1_2L_3Zn_2$. Nevertheless, the configuration of three diarylcyclopentene components manifests obvious changes. In agreement with the information deduced from the UV solution study, among the three PADTE-laterals only one is converted into the ring-closed state, resulting in a reduced C–C distance of 1.52 Å to connect two thiophene rings. However the C···C distances on the other open-ring laterals are 3.52 and 3.72 Å, a little increased in comparison with *o*-$A^1_2L_3Zn_2$. In *c*-$A^1_2L_3Zn_2$,- the distance between the two Zn^{2+} centers is 15.99 Å, slightly shorter than that in the open-ring cage. These observations indicate that, after ring-closing of one PADTE-lateral which becomes more rigid to cause constraint of the cage, the other two PADTE-laterals are forced to rearrange with distant orientation of two thiophene rings to release the configuration tension, thereof preventing from ring-closing any longer. Similar results were also obtained for the photoisomerization of *o*-$A^2_2L_3Cd_2$ → *c*-$A^2_2L_3Cd_2$ and *o*-$A^2_2L_3Zn_2$ → *c*-$A^2_2L_3Zn_2$ in both the solution and solid-states (Fig. S47–S61†), of which the single-crystal structure of *c*-$A^2_2L_3Cd_2$ was also analysed, confirming that only one PADTE-lateral is closed (Fig. S54†).

Such a partial *o* → *c* photochromic process can be evidently detected in solution by ^{1}H NMR spectra. As shown in Fig. 3d, although the three PADTE components in *o*-$A^1_2L_3Zn_2$ cannot be differentiated in the NMR time scale owing to the conformational flexibility in the ring-opened state, their disparity in the more rigid *c*-$A^1_2L_3Zn_2$ can be readily distinguished. Upon UV-irradiation of *o*-$A^1_2L_3Zn_2$ in solution, each of the original proton signals in the aromatic ring zone gradually shifts and splits into three sets of peaks, and reaches a steady state after about 90 minutes. This result is consistent with the UV change to deduce that only one of the three PADTE-laterals is closed in *c*-$A^1_2L_3Zn_2$, which makes the three PADTE-laterals in *c*-$A^1_2L_3Zn_2$- unequivalent taking into account the triple-helicate

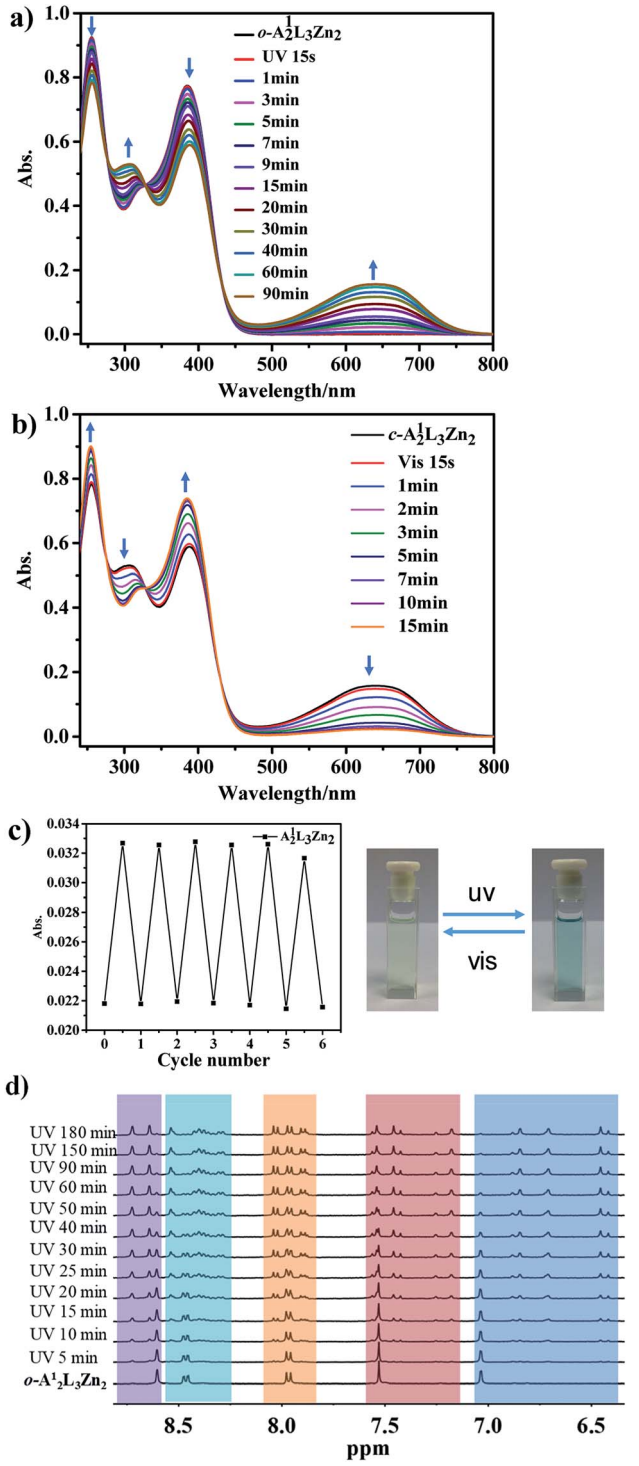

Fig. 3 (a) UV-Vis spectra of *o*-$A^1_2L_3Zn_2$ during ring-closing and (b) *c*-$A^1_2L_3Zn_2$ during the ring-opening process ($CH_3CN/CHCl_3$, v : v = 1 : 1, 1×10^{-5} mol L^{-1}, 298 K). (c) Cycled signals for absorbance at 627 nm during alternate ring-closing/opening processes (left), and color change photos (right). (d) Time-dependent ^{1}H NMR spectral evolution of *o*-$A^1_2L_3Zn_2$ under UV irradiation (400 MHz, CD_3CN, 298 K).

Open Access Article. Published on 06 August 2020. Downloaded on 2/6/2026 6:47:13 AM.
This article is licensed under a Creative Commons Attribution-NonCommercial 3.0 Unported Licence.

arrangement and the ΔΔ- or ΛΛ-homochirality of each cage. High resolution ESI-MS presents the corresponding species of $[A^1_2L_3Zn_2]^{4+}$ (Fig. S44†), also showing the existence of a closed-ring cage structure in solution. From the DOSY spectrum (Fig. S45†), we can calculate the *c*-$A^1_2L_3Zn_2$ sphere to be about 8.5 Å from the *D* value of 7.94 × 10^{-10} m^2 s^{-1}, a little bit smaller than flexible *o*-$A^1_2L_3Zn_2$. It should be indicated that the photoisomerization behaviors for the cages might be complicated in solution. To give more evidence, we compared the NMR spectra of the crystallized sample of *c*-$A^1_2L_3Zn_2$ with the solution sample of *o*-$A^1_2L_3Zn_2$ after UV irradiation (Fig. S46b†), which displayed similar signals. This confirms that most part of the species in the solution after photoisomerization should be the cages with only one lateral closed as confirmed by single crystal XRD analyses, as also supported by MS spectra with the observation of one kind of species. However, in the solution state, it is very likely that multiple species and/or dynamic photoisomerization equilibrium might also exist.

For reverse photoisomerization, the ring-closing process was also manifested by continuous luminescence quenching of the original open-cage upon UV-irradiation, for which the red emission at 635 nm is gradually weakened till almost it disappears (Fig. S43†). This is a little surprising because there are two PADTE components in the ring-opened state, implying that one ring-closure may significantly influence the conformation of the cage and even luminescence behaviour of the other two PADTE components. The back conversion of *c*-$A^1_2L_3Zn_2$ to *o*-$A^1_2L_3Zn_2$ under the irradiation of visible light is also confirmed by UV-Vis spectral evolution, which is completed in 15 minutes (Fig. 3b). By monitoring the absorption intensity swaps at 627 nm, cyclic experiments were carried out under alternate irradiation of ultraviolet and visible light. After six cycles, the absorption changing tendency and amplitude remain basically stable, proving that the structural transformation between *c*-$A^1_2L_3Zn_2$ and *o*-$A^1_2L_3Zn_2$ has good cyclability (Fig. 3c).

Covalent cages

The reversible photoisomerization processes of *o*-R-$A^1_2L_3$ were explored under similar conditions (Fig. 4 and S62–S65†). By UV light irradiation, the solution color is changed from colorless to light purple, and the two absorption peaks related to *o*-R-$A^1_2L_3$ (278 and 320 nm) are gradually weakened, while the two absorption peaks related to *c*-R-$A^1_2L_3$ (376 and 538 nm) are gradually enhanced. After 90 min, the absorption spectrum becomes stable and reaches the ring-closed state (Fig. 4a). To compare with the absorption changing magnitude of PADTE, it was also deduced that only one of the three sides in the covalent cage is closed by UV irradiation. Under visible light irradiation, the absorption spectrum shows an inverted change, corresponding to the ring-close to ring-open conversion, which can be completed in just 180 s (Fig. 4b). Such interconversion processes can be cycled for more than six times without significant reduction in the absorption swapping magnitude (Fig. 4c), indicative of good photostablility of the covalent cage under UV irradiation.

As shown in Fig. 4d, the ^{1}H NMR spectral change of *o*-R-$A^1_2L_3$ in CD_3OD solution was monitored by UV irradiation for

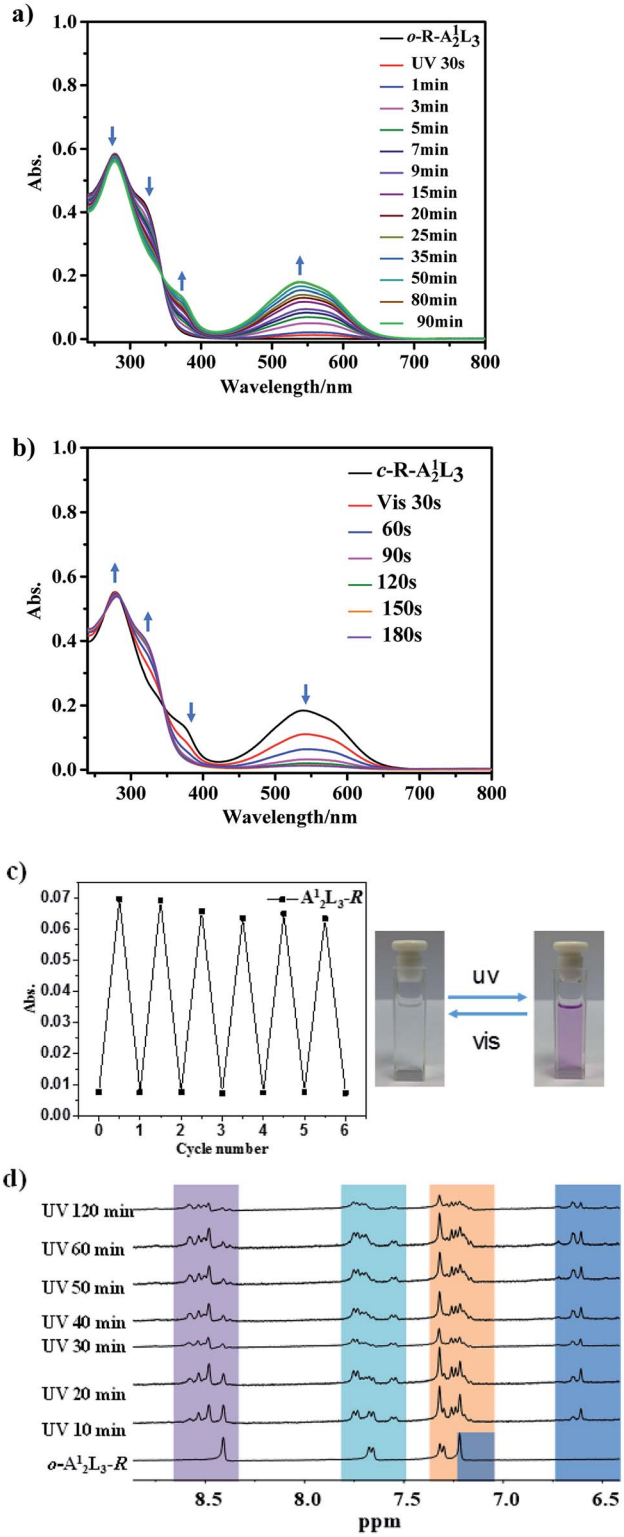

Fig. 4 (a) UV-Vis spectra of *o*-R-$A^1_2L_3$ during ring-closing, and (b) *c*-R-$A^1_2L_3$ during the ring-opening process ($CH_3CN/CHCl_3$, v : v = 1 : 1, 1 × 10^{-5} mol L^{-1}, 298 K). (c) Cycled signals for absorbance at 538 nm during alternative ring-closing/opening processes (left), and color change photos (right). (d) Time-dependent ^{1}H NMR spectral evolution of *o*-R-$A^1_2L_3$ under UV irradiation (400 MHz, CD_3OD, 298 K).

This journal is © The Royal Society of Chemistry 2020

Open Access Article. Published on 06 August 2020. Downloaded on 2/6/2026 6:47:13 AM.
This article is licensed under a Creative Commons Attribution-NonCommercial 3.0 Unported Licence.

different times. We can see that, as the irradiation time increases, the four groups of proton signals in the aromatic ring region gradually split, accompanied by a certain displacement. This indicates that the conformation of diarylcyclopentene skeletons becomes distinguishable along the ring closure reaction. Basically, after 120 min, each set of proton signals for *o*-R-$A^1_2L_3$ is split into three sets of signals assignable to *c*-R-$A^1_2L_3$. This result is similar to that of the corresponding coordinative cages, suggesting that only one of the three cage sides will change into the ring-closed state under UV irradiation. High-resolution mass spectrometry was applied to detect the existence of *c*-R-$A^1_2L_3$ in solution. The major peak in the whole spectrum with $m/z = 804.8492$ can be assigned to the $[(\text{R-}A^1_2L_3) + 2H^+]^{2+}$ species, with perfect agreement between the measured and simulated isotopic distributions (Fig. S63†). The DOSY spectra (Fig. S64†) also manifest that all signals for the *c*-R-$A^1_2L_3$ cage have the same diffusion coefficient, which proves that the product is uniform in solution. Furthermore, the ring-closing process of *o*-R-$A^1_2L_3$ can be detected by its luminescent quenching (Fig. S65†). Different from the red emission of *o*-$A^1_2L_3Zn_2$, *o*-R-$A^1_2L_3$ displays a wide emission around 460 nm, which is also continuously diminished under UV-irradiation until it nearly disappears as observed in *o*-$A^1_2L_3Zn_2$. Similar photoisomerization processes were also found for the covalent cages constructed from the A^2 component (Fig. S66–S72†).

Photoisomerization dynamics of the ligand and cages

The photoisomerization processes of the ligand and cages were then studied using the first-order reaction dynamics. We can use the following equation of the Lambert–Beer law to fit the rate constant,

$$\ln(A_0 - A_\infty)/(A_t - A_\infty) = kt$$

where A_0, A_t, and A_∞ represent the absorbance at the initial, intermediate and final states, t is the radiation time, and k is the rate constant. For the ligand PADTE, we used the absorbance at 605 nm to estimate the ring-opening and ring-closing rate constants of the UV and visible light irradiation processes. For which, two comparable values, 0.826 and 0.793 min^{-1}, were obtained, respectively, suggesting that the forward and backward photochromic conversion rates are comparable for the free ligand under the testing conditions (Table 1).

In comparison, using the absorbance at 627 nm to estimate the rate constants of photo-conversions between coordinative cages *o*-$A^1_2L_3Zn_2$ and *c*-$A^1_2L_3Zn_2$, the values 0.045 and 0.408 min^{-1} were obtained, respectively, which are both reduced compared with those of the PADTE ligand. Particularly, the rate constant for the ring-closing conversion process under UV irradiation is remarkably reduced to about 1/18 of that of the free ligand. This indicates that the steric structure of the cage limits the free rotation of the methyl groups on the two thiophene rings, resulting in a largely slower conversion rate under UV irradiation. The rate constants of 0.041 and 1.301 min^{-1} were obtained for the conversions between open-and closed-states of organic cages *o*-R-$A^1_2L_3$ and *c*-R-$A^1_2L_3$ by detecting the absorbance at 538 nm. Compared to the free ligand and coordinative cages, the conversion speed from the ring-open state to the ring-closed state slows down, but the speed from the ring-closed state to the ring-open state increases dramatically. This implies that the covalent cage prefers the ring-open state much more than the ring-closed state, probably due to the change of the linking mode between A and L moieties from C=N imine bonds to C–NH amine bonds. Meanwhile, based on the present results, it seems that the introduction of a flexible linker into the coordination cages and COCs does not lead to a consistent effect for the photoswitching behavior. As can be seen from Table 1, keeping the same Zn template and changing A^1 to A^2, the coordination cage will show larger $k_{closing}$ and smaller $k_{opening}$, while for the COC configuration, when changing A^1 to A^2, the tendency is just the opposite. More detailed and systematic experiments will be performed in the future for further exploration along this line.

Furthermore, the photoisomerization process of the organic cage can be modulated by the encapsulated guests. Since the metal-free covalent cage has a large cavity which is empty and possesses two binding spheres surrounded by seven N atoms at both ends of the cage, suitable guest molecules or anions may be encapsulated through hydrogen bonding, thereof affecting the photodynamic process. To test this, different amounts of HSO_4^- or $H_2PO_4^-$ anions were added into the CH_2Cl_2 solution of *o*-R-$A^1_2L_3$, and the ring-closing photochromic conversion behaviour was monitored by the naked eye color observation and UV-Vis spectroscopy. As shown in Fig. S73 and S74,† the anions indeed act like a dimmer control to tune down the color of the solution, and the characteristic absorption peak (538 nm) assignable to the closed-ring form of *c*-R-$A^1_2L_3$ is decreased with the increased amount of $H_2PO_4^-$ or HSO_4^- after 90 minute UV irradiation. This suggests that the guest anions are combined into the cages *via* formation of hydrogen bonding with N atoms, which has been verified by NMR titration to show gradual displacement of the chemical shift signals along $H_2PO_4^-$ or

Table 1 Photoisomerization dynamic rates for the ligand and cages

Attribution	Compound	$k_{closing}$ [min^{-1}] (365 nm)	$k_{opening}$ [min^{-1}] (>455 nm)
Ligand	PADTE	0.826	0.793
Coordinative cages	$A^1_2L_3Zn_2$	0.045	0.408
	$A^2_2L_3Cd_2$	0.140	0.434
	$A^2_2L_3Zn_2$	0.093	0.392
Covalent cages	R-$A^1_2L_3$	0.041	1.301
	R-$A^2_2L_3$	0.030	1.552

Open Access Article. Published on 06 August 2020. Downloaded on 2/6/2026 6:47:13 AM.
This article is licensed under a Creative Commons Attribution-NonCommercial 3.0 Unported Licence.

HSO_4^- addition (Fig. S75 and S76†). It is to be expected that the more anions are added, the tighter host-guest binding is preferred due to guest exchange equilibrium. As a consequence, the rotation of the diaryl skeleton becomes more restricted, which may make the photoisomerization process sluggish.

Application of the photochromic cages in color-tuning for logic gate models

Up-conversion materials can emit visible light photoluminescence when excited in the near-infrared (NIR) region, and are widely applicable in biomarkers, cell imaging, and safety labels.[46–48] As a preliminary test of application, we combine our photochromic cages with lanthanide-based upconversion materials in order to achieve multi-color modulation by different irradiation.[49–51] For the sake of clarity, we can compare the UV-Vis absorption spectra of the PADTE ligand and the coordinative/covalent cages in the ring-closed state with the emission spectra of upconversion materials Er-1, Er-5 and Er-9 (macroporous ZrO_2 : Er(III)–Yb(III) materials with different Er/Yb molar ratios of 1 : 1, 1 : 5 and 1 : 9, see preparation details in the ESI, Section 2.7, Fig. S77–S80†). As shown in Fig. 5a, Er-1 can emit both green (maximized at 544 nm) and red (maximized at 679 nm) upconversion PL under NIR excitation, resulting in an overall greenish-yellow color. However both the *c*-PADTE ligand and *c*-$A^1_2L_3Zn_2$ coordinative cage show a broad absorption band in a range of 480–750 nm (Fig. 5a and S77†). The overlapped parts between the absorption band of *c*-PADTE or *c*-$A^1_2L_3Zn_2$ and the green and red upconversion emissions of Er-1 are nearly equivalent. So it is speculated that, after mixing *c*-PADTE or *c*-$A^1_2L_3Zn_2$ with Er-1, the intensity of the upconverted red and green light of Er-1 will be simultaneously reduced in comparable proportion to the absorption of *c*-PADTE or *c*-$A^1_2L_3Zn_2$ in these two regions. Therefore, an overall color attenuation of the upconversion PL will be discerned. In contrast, since the absorption band of the ring-closed form of covalent cage *c*-R-$A^1_2L_3$ is blue-shifted to 450–700 nm, the absorption in the green light region is obviously stronger than that in the red light region of Er-1 (Fig. 5a and S77†). Consequently, *c*-R-$A^1_2L_3$ can act as a selective light absorber to discriminate the red and green emissions of Er-1, leading to PL color-tuning of the upconverted materials.

In order to testify the above speculation, 0.11% mass fraction of *o*-R-$A^1_2L_3$ was mixed with three kinds of upconversion materials Er-1, Er-5 and Er-9 which themselves emit an overall greenish-yellow, orange and red upconversion light, respectively. As demonstrated in Fig. 5b and S78,† after adding *o*-R-$A^1_2L_3$ and irradiating the mixed materials with UV light, the colors of the hybrid materials change from white to purple due to continuous formation of *c*-R-$A^1_2L_3$ to show increased absorption in the visible region. Meanwhile, when NIR excitation at 980 nm is applied, the green upconversion emission of the hybrid materials is significantly diminished owing to absorption of the emission light by *c*-R-$A^1_2L_3$, but the red emission remains almost unchanged. Therefore, the overall luminescent color is red-shifted. Among them, the light filtering effect of *c*-R-$A^1_2L_3$ on Er-1 is the most distinctive (Fig. S78†), changing the PL

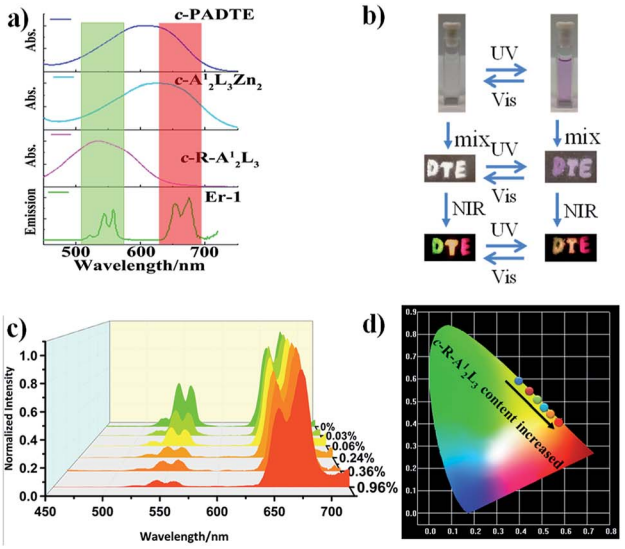

e)

input		Output I	Output II	Output III
o-R-$A^1_2L_3$ 0.11%	UV light 365nm	Without NIR irradiated	With NIR irradiated	
		By the naked eye	By the naked eye	By I_{562}/I_{655} value
0	0	0 (white)	1 (greenish-yellow)	1 (0.54, high)
0	1	0 (white)	1 (greenish-yellow)	1 (0.54, high)
1	0	0 (white)	1 (greenish-yellow)	1 (0.79, high)
1	1	1 (purple)	0 (orange)	0 (0.09, low)

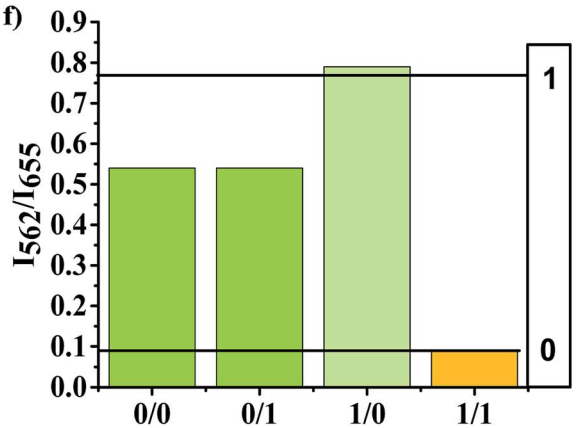

Fig. 5 (a) Overlap between the upconversion emissions of Er-1 and the UV-Vis absorption of *c*-PADTE, *c*-$A^1_2L_3Zn_2$ and *c*-R-$A^1_2L_3$. (b) Color change processes by UV- or Vis-irradiation of *o*/*c*-R-$A^1_2L_3$ (upper), hybrid materials of R-$A^1_2L_3$@Er-1 (for D), R-$A^1_2L_3$@Er-5 (for T) and R-$A^1_2L_3$@Er-9 (for E) under daylight (middle), and 980 nm-NIR excitation (lower). (c) Upconversion emission spectra and (d) CIE coordinates of hybrid materials by adding different ratios of *c*-R-$A^1_2L_3$ (0–0.96%). (e) The truth table for AND and NAND logic gates designed from the *o*-R-$A^1_2L_3$-0.11%@Er-1 system and (f) the corresponding PL readout signals for output III.

This journal is © The Royal Society of Chemistry 2020

Open Access Article. Published on 06 August 2020. Downloaded on 2/6/2026 6:47:13 AM.
This article is licensed under a Creative Commons Attribution-NonCommercial 3.0 Unported Licence.

color from greenish-yellow to orange, which can be clearly detected by the naked eye (Fig. 5b). For comparison, *c*-$A^1_2L_3$-Zn_2 was also mixed with Er-1, Er-5 and Er-9 individually in different ratios to obtain nine kinds of hybrid materials. The upconversion emission spectra show that, as the mass fractions of *c*-$A^1_2L_3Zn_2$ increase, the luminescence intensities are simultaneously decreased with almost equivalent filtering of the red and green lights, leading to general attenuation of luminescence colors (Fig. S79†).

Based on the above observations, multi-readout logic gate operating systems may be envisaged from the visual and PL color changes correlating with the ring closing–opening transitions under UV-Vis and NIR irradiations. As shown in Fig. 5c and d, when different mass fractions of *c*-R-$A^1_2L_3$ were mixed with Er-1, the upconversion PL color can be tuned gradually. As the added *c*-R-$A^1_2L_3$ content is increased, the absorption in the green region is enhanced, thus filtering more green emission to adjust the overall luminescence from greenish-yellow to orange. If both the absorption color changes and the upconversion PL color changes under different light irradiations are considered as on/off operations, we can design a multiple-readable logic gate as shown in Fig. 5e and f. For an *o*/*c*-R-$A^1_2L_3$@Er-1 system, the *o*-R-$A^1_2L_3$ addition and UV irradiation are considered as inputs, and the changes of the absorption color or upconversion PL color are used as the output modes I or II, respectively. For the inputs, the presence and absence of *o*-R-$A^1_2L_3$ or UV irradiation are defined as "1" and "0", respectively.

For output I (without NIR excitation), we can define the eye-detected white color of *o*-R-$A^1_2L_3$ as "0", while the purple color of transformed *c*-R-$A^1_2L_3$ as "1". According to the photoisomerization behavior discussed above, only the presence of both inputs (1/1) could cause a visual color change from white to purple (output "0" → "1"). In this way, an "AND" logic gate is represented. However for output II (with NIR excitation), we define the eye-detectable orange and greenish-yellow upconversion PL colors as output "0" and "1", respectively. As for the photochromic and PL color-tuning behaviors discussed above, in the absence of both inputs (0/0) or in the presence of only one input (1/0, 0/1), output "1" will be obtained (greenish-yellow upconversion PL). Once both inputs are present (1/1), an orange upconversion PL is generated to give output "0". This represents a "NAND" logic gate. The above output I and II are both readable by the naked eye. Since output II originated from the green emission filtering of Er-1, this NAND gate can be further encoded into an instrument readable output III. In which, by detecting the upconversion PL spectra of the sample under 980 nm laser excitation (Fig. S80†), a higher (output "1") or lower (output "0") I_{562}/I_{655} value will be obtained under different input conditions. Only with the presence of both inputs (1/1), an output "0" can be achieved, qualified for a "NAND" operation. In these ways, multi-readable and resettable logic function processors may be designed with good recyclability (Fig. S81†).

Conclusions

By self-assembly of preorganized metallo-components, $A_2L_3M_2$ type coordinative cages have been successfully constructed from photochromic dithienylethene-containing PADTE (L) aldehyde and two tripodal tris-amine (A^1 or A^2) ligands, which are further demetalated by facile reduction into pure organic cages. Both coordinative and covalent cages are endowed with photochromic properties inherited from the PADTE components. Owing to different spatial tension effects in the free ligand and triple-helicated coordinative to covalent cages, distinct photoisomerization dynamics are resulted, although only one of the three lateral sides in the cages is closed under UV irradiation. Differentiating UV-Vis absorption, photoluminescence and interconversion behaviors are observed between the coordinative and organic cages. In combination with lanthanide-based upconversion materials, the coordinative cages play a role of color attenuation, while the organic cages can act as selective light absorbers to tune upconversion PL colors. Furthermore, the photoisomerization process of covalent cages is applied in modulating the absorption and PL colors, providing on/off operations to construct multiple visual and instrumental readable logic gate systems including AND and NAND operations. This study presents a synthetic pathway toward organization of well-defined covalent architectures incorporating functional components without tedious *de novo* organic synthesis, thus bringing about new perspectives in the structural design, mechanism understanding and potential application of complicated and functional organic architectures.

Conflicts of interest

There are no conflicts to declare.

Acknowledgements

This work was supported by the NSFC Projects (21771197, 21890380, 21720102007, and 21821003), and the Local Innovative and Research Teams Project of the Guangdong Pearl River Talents Program (2017BT01C161). We thank Prof. J.-M. Lehn for helpful discussion.

References

1 J. Mosquera, S. Zarra and J. R. Nitschke, *Angew. Chem., Int. Ed.*, 2014, **53**, 1556–1559.
2 X. Yan, M. Wang, T. R. Cook, M. Zhang, M. L. Saha, Z. Zhou, X. Li, F. Huang and P. J. Stang, *J. Am. Chem. Soc.*, 2016, **138**, 4580–4588.
3 C.-L. Liu, R.-L. Zhang, C.-S. Lin, L.-P. Zhou, L.-X. Cai, J.-T. Kong, S.-Q. Yang, K.-L. Han and Q.-F. Sun, *J. Am. Chem. Soc.*, 2017, **139**, 12474–12479.
4 M. Zhang, M. L. Saha, M. Wang, Z. Zhou, B. Song, C. Lu, X. Yan, X. Li, F. Huang, S. Yin and P. J. Stang, *J. Am. Chem. Soc.*, 2017, **139**, 5067–5074.
5 L. Cao, P. Wang, X. Miao, Y. Dong, H. Wang, H. Duan, Y. Yu, X. Li and P. Stang, *J. Am. Chem. Soc.*, 2018, **140**, 7005–7011.
6 J. Jiao, Z. Li, Z. Qiao, X. Li, Y. Liu, J. Dong, J. Jiang and Y. Cui, *Nat. Commun.*, 2018, **9**, 4423.

Open Access Article. Published on 06 August 2020. Downloaded on 2/6/2026 6:47:13 AM.
This article is licensed under a Creative Commons Attribution-NonCommercial 3.0 Unported Licence.

7 M. Pan, K. Wu, J.-H. Zhang and C.-Y. Su, *Coord. Chem. Rev.*, 2019, **378**, 333–349.
8 D. Zhang, T. K. Ronson, J. L. Greenfield, T. Brotin, P. Berthault, E. Leonce, J. L. Zhu, L. Xu and J. R. Nitschke, *J. Am. Chem. Soc.*, 2019, **141**, 8339–8345.
9 Y. Zhao, L. Zhang, X. Li, Y. Shi, R. Ding, M. Teng, P. Zhang, C. Cao and P. J. Stang, *Proc. Natl. Acad. Sci. U. S. A.*, 2019, **116**, 4090–4098.
10 D. Luo, X.-P. Zhou and D. Li, *Angew. Chem., Int. Ed.*, 2015, **54**, 6190–6195.
11 D. Luo, X.-Z. Wang, C. Yang, X.-P. Zhou and D. Li, *J. Am. Chem. Soc.*, 2018, **140**, 118–121.
12 X. Zhang, X. Dong, W. Lu, D. Luo, X.-W. Zhu, X. Li, X.-P. Zhou and D. Li, *J. Am. Chem. Soc.*, 2019, **141**, 11621–11627.
13 X.-Z. Li, L.-P. Zhou, L.-L. Yang, D.-Q. Yuan, C.-S. Lin and Q.-F. Sun, *J. Am. Chem. Soc.*, 2017, **139**, 8237–8244.
14 L.-X. Cai, L.-L. Yan, S.-C. Li, L.-P. Zhou and Q.-F. Sun, *Dalton Trans.*, 2018, **47**, 14204–14210.
15 E. Fazio, C. J. E. Haynes, G. de la Torre, J. R. Nitschke and T. Torres, *Chem. Commun.*, 2018, **54**, 2651–2654.
16 J.-F. Ayme, J. E. Beves, C. J. Campbell and D. A. Leigh, *J. Am. Chem. Soc.*, 2019, **141**, 3605–3612.
17 D. Zhang, T. K. Ronson and J. R. Nitschke, *Acc. Chem. Res.*, 2018, **51**, 2423–2436.
18 T. Zhang, G.-L. Zhang, Q.-Q. Yan, L.-P. Zhou, L.-X. Cai, X.-Q. Guo and Q.-F. Sun, *Inorg. Chem.*, 2018, **57**, 3596–3601.
19 A. J. Plajer, E. G. Percastegui, M. Santella, F. J. Rizzuto, Q. Gan, B. W. Laursen and J. R. Nitschke, *Angew. Chem., Int. Ed.*, 2019, **58**, 4200–4204.
20 L. Zhao, X. Jing, X. Li, X. Guo, L. Zeng, C. He and C. Duan, *Coord. Chem. Rev.*, 2019, **378**, 151–187.
21 M. Pan and C.-Y. Su, *CrystEngComm*, 2014, **16**, 7847–7859.
22 A. B. Pun, K. J. Gagnon, L. M. Klivansky, S. J. Teat, Z. T. Li and Y. Liu, *Org. Chem. Front.*, 2014, **1**, 167–175.
23 L. Zhang, L. Lin, D. Liu, Y.-J. Lin, Z.-H. Li and G.-X. Jin, *J. Am. Chem. Soc.*, 2017, **139**, 1653–1660.
24 T. Sawada, M. Yamagami, K. Ohara, K. Yamaguchi and M. Fujita, *Angew. Chem., Int. Ed.*, 2016, **55**, 4519–4522.
25 L. Yang, X. Jing, B. An, C. He, Y. Yang and C. Duan, *Chem. Sci.*, 2018, **9**, 1050–1057.
26 R. Zhu, I. Regeni, J. J. Holstein, B. Dittrich, M. Simon, S. Prevost, M. Gradzielski and G. H. Clever, *Angew. Chem., Int. Ed.*, 2018, **57**, 13652–13656.
27 M. M. Siddiqui, R. Saha and P. S. Mukherjee, *Inorg. Chem.*, 2019, **58**, 4491–4499.
28 G. Yu, D. Wu, Y. Li, Z. Zhang, L. Shao, J. Zhou, Q. Hu, G. Tang and F. Huang, *Chem. Sci.*, 2016, **7**, 3017–3024.
29 J. Y. C. Lim, I. Marques, A. L. Thompson, K. E. Christensen, V. Felix and P. D. Beer, *J. Am. Chem. Soc.*, 2017, **139**, 3122–3133.
30 M. Kaeseborn, J. J. Holstein, G. H. Clever and A. Luetzen, *Angew. Chem., Int. Ed.*, 2018, **57**, 12171–12175.
31 J. Y. C. Lim, I. Marques, V. Felix and P. D. Beer, *Angew. Chem., Int. Ed.*, 2018, **57**, 584–588.
32 M. Kolodziejski, A. R. Stefankiewicz and J. M. Lehn, *Chem. Sci.*, 2019, **10**, 1836–1843.
33 T. Jiao, G. Wu, L. Chen, C.-Y. Wang and H. Li, *J. Org. Chem.*, 2018, **83**, 12404–12410.
34 K. Acharyya and P. S. Mukherjee, *Angew. Chem., Int. Ed.*, 2019, **58**, 8640–8653.
35 X. Zheng, W. Zhu, C. Zhang, Y. Zhang, C. Zhong, H. Li, G. Xie, X. Wang and C. Yang, *J. Am. Chem. Soc.*, 2019, **141**, 4704–4710.
36 M. Estrader, J. S. Uber, L. A. Barrios, J. Garcia, P. Lloyd-Williams, O. Roubeau, S. J. Teat and G. Aromi, *Angew. Chem., Int. Ed.*, 2017, **56**, 15622–15627.
37 R. Kashihara, M. Morimoto, S. Ito, H. Miyasaka and M. Irie, *J. Am. Chem. Soc.*, 2017, **139**, 16498–16501.
38 D. E. Williams, C. R. Martin, E. A. Dolgopolova, A. Swifton, D. C. Godfrey, O. A. Ejegbavwo, P. J. Pellechia, M. D. Smith and N. B. Shustova, *J. Am. Chem. Soc.*, 2018, **140**, 7611–7622.
39 J. J. Xu, H. Volfova, R. J. Mulder, L. Goerigk, G. Bryant, E. Riedle and C. Ritchie, *J. Am. Chem. Soc.*, 2018, **140**, 10482–10487.
40 K. Z. Zheng, S. Y. Han, X. Zeng, Y. M. Wu, S. Y. Song, H. J. Zhang and X. G. Liu, *Adv. Mater.*, 2018, **30**, 5.
41 Z. Y. Li, J. W. Dai, M. Damjanovic, T. Shiga, J. H. Wang, J. Zhao, H. Oshio, M. Yamashita and X. H. Bu, *Angew. Chem., Int. Ed.*, 2019, **58**, 4339–4344.
42 M. Han, R. Michel, B. He, Y.-S. Chen, D. Stalke, M. John and G. H. Clever, *Angew. Chem., Int. Ed.*, 2013, **52**, 1319–1323.
43 R. J. Li, J. J. Holstein, W. G. Hiller, J. Andreasson and G. H. Clever, *J. Am. Chem. Soc.*, 2019, **141**, 2097–2103.
44 R. J. Li, M. Han, J. Tessarolo, J. J. Holstein, J. Lubben, B. Dittrich, C. Volkmann, M. Finze, C. Jenne and G. H. Clever, *ChemPhotoChem*, 2019, **3**, 378–383.
45 E. S. Tam, J. J. Parks, W. W. Shum, Y.-W. Zhong, M. E. B. Santiago-Berríos, X. Zheng, W. Yang, G. K.-L. Chan, H. D. Abruna and D. C. Ralph, *ACS Nano*, 2011, **5**, 5115–5123.
46 F. Wang, R. Deng, J. Wang, Q. Wang, Y. Han, H. Zhu, X. Chen and X. Liu, *Nat. Mater.*, 2011, **10**, 968.
47 D. Wang, L. Zhu, J.-F. Chen and L. Dai, *Angew. Chem., Int. Ed.*, 2016, **55**, 10795–10799.
48 G. Chen, J. Shen, T. Y. Ohulchanskyy, N. J. Patel, A. Kutikov, Z. Li, J. Song, R. K. Pandey, H. Ågren, P. N. Prasad and G. Han, *ACS Nano*, 2012, **6**, 8280–8287.
49 T. Q. Wu, J. C. Boyer, M. Barker, D. Wilson and N. R. Branda, *Chem. Mater.*, 2013, **25**, 2495–2502.
50 H.-B. Cheng, G.-F. Hu, Z.-H. Zhang, L. Gao, X. Gao and H.-C. Wu, *Inorg. Chem.*, 2016, **55**, 7962–7968.
51 J.-C. Boyer, C.-J. Carling, B. D. Gates and N. R. Branda, *J. Am. Chem. Soc.*, 2010, **132**, 15766–15772.

 This journal is © The Royal Society of Chemistry 2020